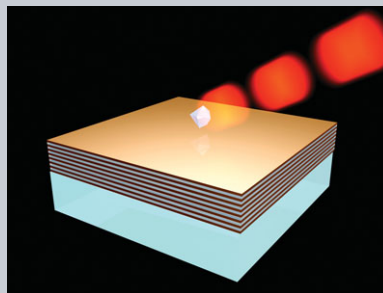


Abstract The broadband enhancement of single-photon emission from nitrogen-vacancy centers in nanodiamonds coupled to a planar multilayer metamaterial with hyperbolic dispersion is studied experimentally. The metamaterial is fabricated as an epitaxial metal/dielectric superlattice consisting of CMOS-compatible ceramics: titanium nitride (TiN) and aluminum scandium nitride ($\text{Al}_x\text{Sc}_{1-x}\text{N}$). It is demonstrated that employing the metamaterial results in significant enhancement of collected single-photon emission and reduction of the excited-state lifetime. Our results could have an impact on future CMOS-compatible integrated quantum sources.



Enhancement of single-photon emission from nitrogen-vacancy centers with TiN/(Al,Sc)N hyperbolic metamaterial

Mikhail Y. Shalaginov^{1,2,**}, Vadim V. Vorobyov^{3,4,**}, Jing Liu⁵, Marcello Ferrera^{1,2,7}, Alexey V. Akimov^{4,6,8}, Alexei Lagutchev², Andrey N. Smolyaninov³, Vasily V. Klimov^{3,8}, Joseph Irudayaraj⁵, Alexander V. Kildishev^{1,2}, Alexandra Boltasseva^{1,2}, and Vladimir M. Shalaev^{1,2,*}

1. Introduction

Generation and detection of single photons play an important role in both fundamental and applied aspects of quantum photonics. The concept of photon lies at the foundation of quantum theory of light, and it is a workhorse of quantum information processing [1], including quantum computation [2], quantum cryptography [3], quantum communication [4] and teleportation [5]. Over the past ten years, numerous types of microscopic, truly deterministic single-photon sources have been demonstrated [6], including trapped atoms [7] and ions [8], single molecules [9], color centers [10], atomic ensembles [11], quantum dots [12], and mesoscopic quantum wells [13].

A nitrogen-vacancy (NV) color center in diamond, formed by a substitutional nitrogen atom and a vacancy at an adjacent lattice site, is of particular interest for photonic quantum technologies [14]. As a single-photon source, it is resistant against photobleaching and operates in the single-photon regime at room temperature [15]. Additionally, its intrinsic quantum yield is close to unity [14], it can be well

localized, and its optical transition can be tuned via external electric [16] and/or magnetic fields [17].

Diamond NV centers have also gained significant attention as a promising solid-state spin system. Its electron spin state has a coherence time in the range of milliseconds at room temperature [18] and can be read out optically [19]. This unique spin-photon interface enables the construction of fault-tolerant quantum-memory units [20] and high-fidelity single-shot projective measurement of single nuclear spins [21]. Moreover, NV centers as solid-state structures hold enormous potential in sharing quantum entanglement among a large number of qubits [22] and implementing scalable quantum-information systems [23]. Nitrogen-vacancy centers could also be used as sensors of electric [24] and magnetic [25] fields, temperature [26] and/or rotation [27] with high resolution and sensitivity.

The applications of an NV center as a single-photon generator and spin-photon interface could substantially benefit from an enhanced emission rate and collection efficiency. The improvement of collection efficiency was

¹ School of Electrical and Computer Engineering, Purdue University, West Lafayette, IN 47907, USA

² Birck Nanotechnology Center, Purdue University, West Lafayette, IN 47907, USA

³ Photonic Nano-Meta Technologies, ul. Lugovaya 4, Skolkovo Innovation Center, Moscow, 143026, Russia

⁴ Moscow Institute of Physics and Technology, Institutskiy per. 9, Dolgoprudny, Moscow Region, 141700, Russia

⁵ Agricultural and Biological Engineering, Purdue University, West Lafayette, IN 47907, USA

⁶ Russian Quantum Center, ul. Novaya 100, BC "Ural", Skolkovo Innovation Center, Moscow Region, 143025, Russia

⁷ School of Engineering and Physical Sciences, Heriot-Watt University, Edinburgh, Scotland, EH14 4AS, United Kingdom

⁸ Lebedev Physical Institute RAS, Leninskij pr. 53, Moscow, 119991, Russia

**These authors contributed equally to this work.

*Corresponding author: E-mail: shalaev@purdue.edu

demonstrated by using solid immersion lenses [28, 29], diamond nanoposts [30], and various grating structures [31]. An emission rate enhancement can be achieved by engineering the electromagnetic environment of the emitter utilizing the Purcell effect [32]. So far, this has been accomplished by using resonant photonic structures, such as microspherical resonators [33], photonic crystal microcavities [34, 35], and photonic crystal nanobeams [36], which are all bandwidth limited.

Coupling NV centers to hyperbolic metamaterials (HMM) [37–40] allows for alteration of the spontaneous decay rate of single-photon emitters over a broad spectral range. This is possible because of a drastic increase in the local density of states (LDOS) provided by HMM. This creates numerous extra decay channels for the coupled emitter [41–46]. The excitation is transferred into high- k metamaterial modes which result from hybridization of surface plasmon polaritons at the interfaces of the layers constituting the HMM. For the perfect planar HMM structure, the excitation in these modes is eventually lost to absorption. However, since it is possible to outcouple these metamaterial modes into free space, they could significantly contribute to the emission signal [44, 47]

Previously, we have shown that the emission from multiple NV centers in nanodiamonds could be enhanced over a broad wavelength range by using multilayer hyperbolic metamaterials, fabricated as a stack of alternating layers of gold and alumina [48]. In this work, we report the next step towards the construction of an efficient on-chip CMOS-compatible single-photon source by replacing gold with semiconductor-compatible plasmonic ceramics [49, 50] as an HMM material building block. Here, we investigate single-NV-center nanodiamonds, which are coupled to an epitaxially grown metamaterial superlattice composed of titanium nitride (TiN) as a plasmonic material and aluminum scandium nitride ($\text{Al}_x\text{Sc}_{1-x}\text{N}$) as a dielectric [50].

TiN is a new plasmonic material known for its CMOS compatibility, mechanical strength, and thermal stability at high temperatures (melting point $>2700^\circ\text{C}$) [51, 52]. This material can be uniformly deposited on a variety of different substrates, such as magnesium oxide, silicon, aluminum scandium nitride, and c-sapphire, in the form of ultra-thin (<5 nm) epitaxial films. This is of fundamental importance for achieving a significant increase in LDOS, since the LDOS for a multilayer HMM is inversely related to the cube of the metamaterial period [53, 54].

2. Experiment

An aqueous suspension of nanodiamonds with nominal size of 50 nm, 0.5% w/v was obtained from Microdiamant AG (MSY 0.05, GAF). According to previous studies, nanodiamonds with the size of 50–70 nm showed the highest probability to host a single NV center [55]. Undersized nanodiamonds and impurities were eliminated by centrifuging at 5000 rpm for 5 minutes followed by supernatant (80%

volume fraction) replacement with distilled water. After that, the suspension was shaken until it became homogeneous. The described procedure was repeated 5 times. Subsequently, a 20 μl drop of the processed suspension was spin-coated onto a superlattice sample at 2000 rpm for 2 minutes. This procedure resulted in nanodiamonds with average size close to 50 nm as shown by the SEM scan in Fig. 1(a). Finally, the sample was covered with a 60-nm-thick layer of polyvinyl alcohol (PVA, 1.5% w/v) to immobilize and separate nanodiamonds from the immersion oil. The immersion oil was required for efficient collection of emitted light by an objective lens with the high numerical aperture.

For reference purposes nanodiamonds were deposited by the same method onto standard 150- μm -thick glass coverslips (VWR VistaVision™ Cover Glasses, No. 1). Since the refractive indices of these glass substrates (1.53), immersion oil (1.52) and PVA layer (1.50) [56] are close, the nanodiamonds in the reference samples were effectively immersed into an infinite homogeneous medium with a refractive index of 1.5. Detailed studies of spontaneous emission enhancement for emitters placed on TiN/(Al,Sc)N superlattice HMMs as compared to TiN films as reference samples are discussed in [50].

A TiN/ $\text{Al}_{0.7}\text{Sc}_{0.3}\text{N}$ superlattice was epitaxially grown on a 0.5-mm-thick, [001]-oriented magnesium oxide (MgO) substrate using reactive DC magnetron sputtering (PVD Products) with a base pressure of 10^{-7} torr at 750°C . The metamaterial was fabricated as an epitaxial stack of 10 pairs of layers each consisting of an 8.5-nm-thick film of TiN and a 6.3-nm-thick film of $\text{Al}_{0.7}\text{Sc}_{0.3}\text{N}$ similar to the approach described in [50]. Fig. 1(b) demonstrates the cross-sectional TEM image of the superlattice. The sample consisted of the described superlattice with nanodiamonds placed on top as shown in Fig. 1(c). Since the superlattice layer thicknesses are much smaller than the operational wavelength (600–800 nm), the HMM can be approximated as a uniaxial anisotropic effective medium with dielectric functions ε_{\parallel} and ε_{\perp} [57]. The optical constants of the HMM were measured using spectroscopic ellipsometry (J. A. Woollam Co.; W-VASE) [58]. The details of the fitting are given in the Supporting Information S1. The TiN/(Al,Sc)N metamaterial exhibited hyperbolic dispersion with $\varepsilon_{\perp} = 16.4 + i21.1$, $\varepsilon_{\parallel} = -2.3 + i2.1$ at 685 nm, which is in the wavelength range of the NV center emission (600–800 nm, Fig. 2, highlighted area). Thus, for the electric field, which is parallel to the interface, the metamaterial at this wavelength behaved as a metal. As an additional benefit, at the excitation wavelength of 532 nm (Fig. 2, vertical dashed green line) the TiN/(Al,Sc)N metamaterial behaved as a lossy dielectric with $\varepsilon_{\parallel} = 1.27 + i1.6$. In the given configuration, the excitation field is predominantly parallel to the interface. Therefore, the non-metallic nature of the metamaterial at this wavelength prevents attenuation of the tangential component of electric field at the surface. This facilitates efficient delivery of the excitation field to the NV center. The transmittance, reflectance and absorbance spectra of the HMM are shown in the Supporting Information S2.

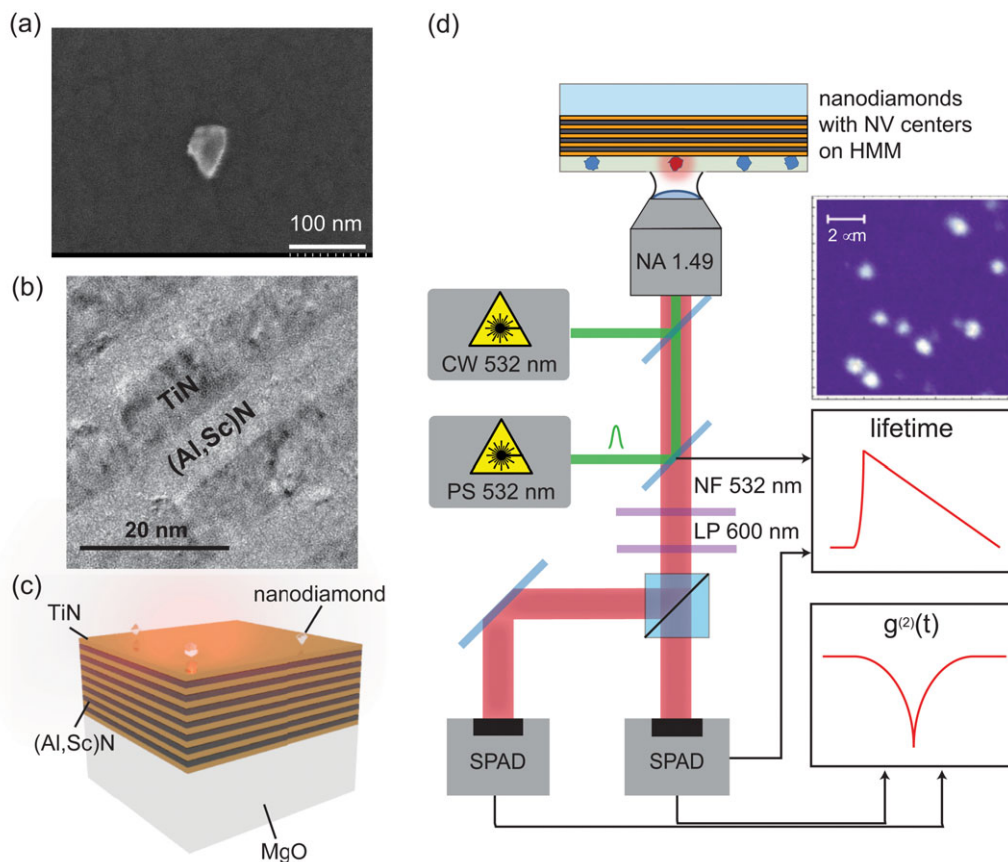


Figure 1 (a) SEM scan of nanodiamonds on top of the HMM sample. Average nanodiamond size is 50 nm. (b) Cross-sectional TEM image of TiN- $\text{Al}_{0.7}\text{Sc}_{0.3}\text{N}$ superlattice. Thicknesses of TiN and $\text{Al}_{0.7}\text{Sc}_{0.3}\text{N}$ layers are 8.5 nm and 6.3 nm, respectively. (c) Sample structure. (d) Schematic of the confocal fluorescence microscope.

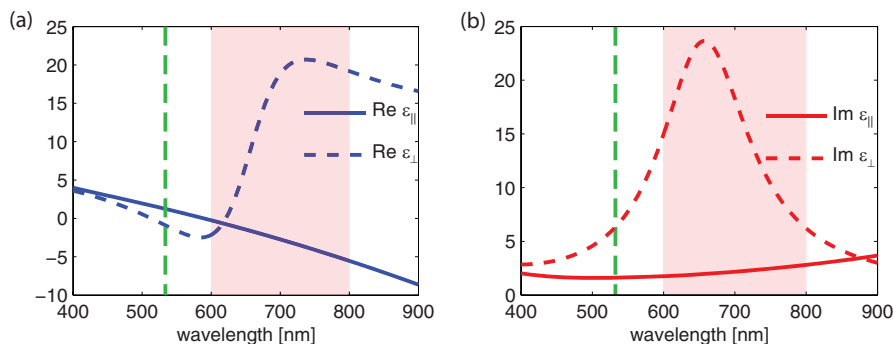


Figure 2 (a) Real and (b) imaginary parts of the dielectric functions of the uniaxial effective medium that approximates the fabricated HMM. The permittivities were obtained by spectroscopic ellipsometry in the spectral range 400 – 900 nm. Within the range of the NV center emission (600–800 nm-highlighted), the metamaterial shows hyperbolic dispersion ($\text{Re}[\epsilon_{\perp}] > 0$, $\text{Re}[\epsilon_{\parallel}] < 0$). At the excitation wavelength (532 nm, green line) the metamaterial behaves as a lossy dielectric.

The enhancement of the spontaneous emission rate and the reduction of the excited state lifetime were investigated using a home-made confocal microscope (Fig. 1(d)). The lifetime measurement procedure was based on time-correlated single photon counting (TCSPC) [59]. The excitation of an NV center for lifetime measurements was performed by a 532-nm pulsed laser (PicoQuant; LDH-P-FA-530XL). Beam scanning across the sample was realized using galvano mirrors (Cambridge Technology; 6215H). The fluorescent radiation from NV centers was collected with a wide aperture ($\text{NA} = 1.49$) oil immersion

lens (Nikon; CFI Apo TIRF 100X Oil) and separated from the excitation radiation by the dichroic mirror (Semrock; LPD01–633RU-25), notch filter (Semrock; NF03–532E-25) and longpass filter (Semrock; LP02–633RU-25). A single-photon avalanche photodiode, SPAD (PerkinElmer; SPCM–AQRH–14–FC) was used as a detector of the NV center single-photon emission. A typical photoluminescence scan of the nanodiamonds with NV centers on top of the glass coverslip is shown in the inset of Fig. 1(d). This setup was converted to a Hanbury Brown–Twiss interferometer [60] to measure the second-order correlation function

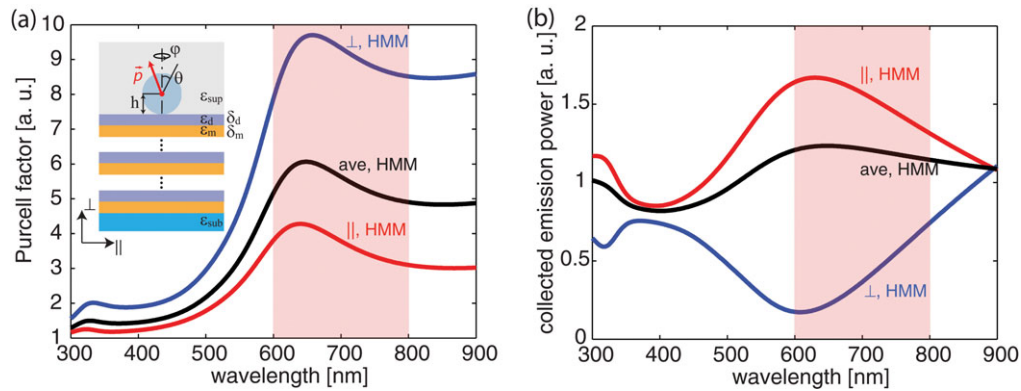


Figure 3 Theoretical estimations of Purcell factor (a) and collected emission power (b) for a dipole located in immersion oil/PVA ($\epsilon_{\text{sup}} = 2.295$) 25 nm above the HMM surface. Blue, red, and black curves correspond to the dipole orientations perpendicular (\perp), parallel (\parallel) to the HMM interface and averaged (ave), respectively. Highlighted area indicates the emission spectral range of NV center at room temperature. Collection angle is 79.6° , which corresponds to NA 1.49. Layout of the calculated structure is shown in the inset.

$g^{(2)}(t)$ by the addition of 50/50 beamsplitter and a second avalanche photodiode connected to a passive signal 80-ns-delay line. In this configuration, the 532 nm continuous-wave laser (Coherent; Compass 315M-100) was used as an excitation source. This measurement was performed to identify nanodiamonds with single NV centers. The value of $g^{(2)}(t)$ was obtained by measuring the background corrected coincidence count rate, normalized by the total counts on each detector, time-bin width and data collection time [61]. The measured dip was fitted with the exponential function of the form $\exp(-[\Gamma + R]|t|)$, where Γ and R are the total decay rate and pump rate, respectively. The signal from the SPAD was processed either by computer counting board (National Instruments; BNC-2121) or by electronic correlation module (PicoHarp 300, PicoQuant).

3. Theory

A straightforward way to estimate both the enhancement of the spontaneous emission rate (represented by Purcell factor F_P) and normalized collected emission power f_{rad} is to utilize a full quantum mechanical treatment. Since in our case the quantum emitter could be considered as weakly coupled to the metamaterial environment, the results are expected to be in a good agreement with the treatment based on the principles of classical electrodynamics [62]. In particular, to model our sample we consider the problem of dipole radiation near a planar layered medium, which is described in more detail in [63–65].

The inset in Fig. 3(a) depicts the modelled configuration, which consists of an oscillating dipole elevated at height h above the HMM uppermost layer ($\text{Al}_{0.7}\text{Sc}_{0.3}\text{N}$), the upper half-space (superstrate) of refractive index 1.515 ($\epsilon_{\text{sup}} = 2.295$ simulating PVA/immersion oil), planar multilayer TiN/(Al,Sc)N superlattice ($\epsilon_{\text{m}}/\epsilon_{\text{d}}$) and the lower half-space (substrate) made of MgO (ϵ_{sub}). For this simulation we considered the fabricated HMM consisting of 10 pairs of 8.5-nm-thick TiN and 6.3-nm-thick $\text{Al}_{0.7}\text{Sc}_{0.3}\text{N}$ on MgO

substrate. The layer thicknesses were chosen to provide optimal performance, which is previously discussed in [50]. The formulas used to calculate the Purcell factor F_P and normalized collected emission power f_{rad} for the dipole orientations: in-plane (\parallel), perpendicular (\perp), and averaged (ave), statistical average over all possible orientations, are given in the Supporting Information S3.

The collection angle ($\theta_{\text{max}} = 79.6^\circ$) is defined by the numerical aperture of the objective lens (NA = 1.49). The generalized Fresnel's reflection coefficients \tilde{r}^{p} and \tilde{r}^{s} for the superlattice were calculated utilizing the recursive imbedding method (see Supporting Information S4), which is more precise and efficient than the direct transfer matrix approach [66]. Normalization factors included into F_P and f_{rad} are the total radiation power and the power emitted into the collection angle, respectively. Both powers corresponded to the case of the emitter immersed into a homogeneous medium with dielectric permittivity ϵ_{sup} , which is a reasonable approximation for the normalization procedure employed in the experiment.

The results of the calculations are demonstrated in Fig. 3. Assuming that the NV center is located at the crystal center, the expected Purcell factor (or change in lifetime) for the nanodiamonds with a mean diameter of 50 nm should be on average around 4.5 (we note that placing NV centers closer to the HMM surface can significantly increase the Purcell factor making it on the order of 10^2 – see Fig. S4(a)). The detected count rates corresponding to the normalized collected emission power for the same type of nanodiamonds are anticipated to increase on average about 1.2 times.

4. Results

In order to select nanodiamonds with single NV centers, we first measured the second-order correlation function $g^{(2)}(t)$ of the detected fluorescence spots. Only NV centers with $g^{(2)}(0)$ significantly less than 0.5 were considered for

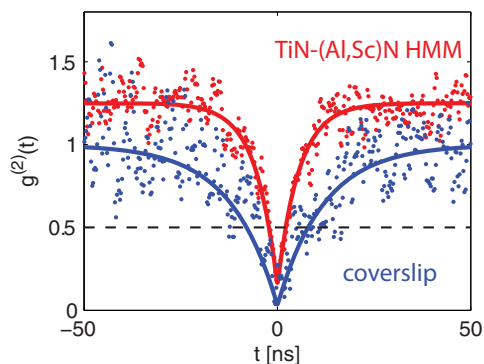


Figure 4 Second-order correlation function $g^{(2)}(t)$ of a representative nanodiamond with single NV center on top of glass coverslip (blue) and HMM (red).

further experiments. The typical photon antibunching effect is shown for a single NV center on the glass coverslip and on the HMM in Fig. 4.

We retrieved the total lifetimes of the NV centers from the exponential fitting of the fluorescence decays such as the ones shown in Fig. 5(a). The average values measured

are 17.1 ns and 4.3 ns on glass and HMM, respectively (see Fig. 5(b)). Hence, the NV centers on HMM exhibit an average decrease in lifetime by a factor of 4, which is consistent with the above calculations. The lowest recorded lifetime for a single NV center on top of HMM is 1.5 ns, which corresponds to a Purcell factor of 11.4. The spreads in the lifetime statistics are likely due to the variation in nanodiamond size, NV center dipole orientation and its distance from the HMM surface (Supporting Information S5).

Finally, we measured the dependence of the single-photon emission rate from the NV centers versus the excitation power. In Fig. 6(a), we show these dependences for the brightest NV centers on both the HMM and the glass coverslip. Both dependences have been corrected for the background emission. The total count rate was measured at the NV center site and the background count rate was measured at a nanodiamond-free location. Saturation of the emission count rate was observed around 1 mW of the pump power. The experimentally measured saturation curves were fitted using the expression $I(P) = I_0 / (1 + P_{sat} / P)$ [67] and yielded the saturated single-photon count rates for each individual NV center. The statistics of these saturated

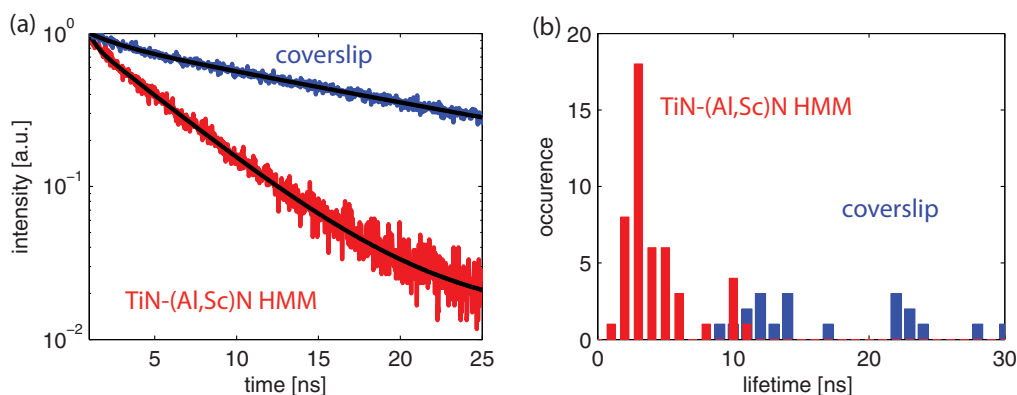


Figure 5 (a) Representative normalized fluorescence decays and (b) histograms of lifetimes for the NV centers located on glass coverslip (blue) and HMM (red). The average and largest decreases in lifetime are 4 and 11.4, respectively.

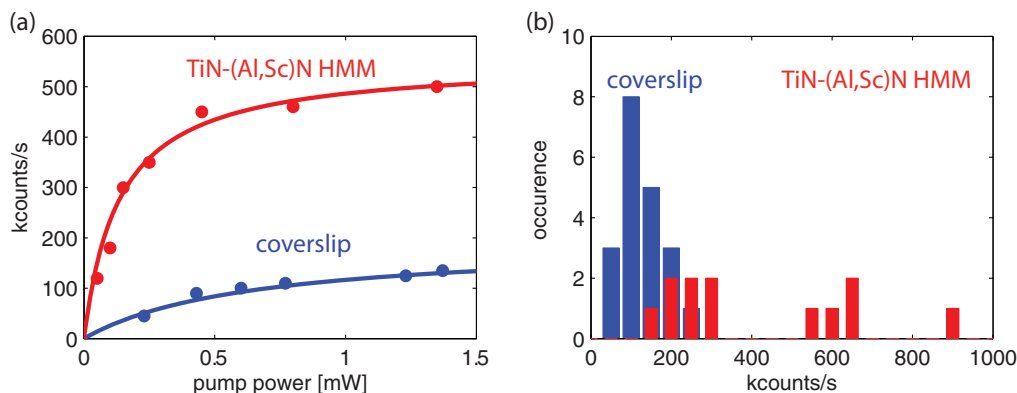


Figure 6 Collected single-photon count rates (corrected for background emission) from NV centers in 50 nm nanodiamonds. (a) Typical saturation curves and (b) histograms of count rates for nanodiamonds on glass coverslip (blue) and HMM (red). The average enhancements for the first and second statistical maxima are 1.8 and 4.7, respectively.

single-photon count rates are shown in Fig. 6(b) for NV centers both on glass and the HMM. It is seen that the measured histogram tends to show multiple maxima. For the one around 200 kcounts/s, the average enhancement against the coverslip was 1.8 ± 1.1 . This is consistent with predicted value of 1.2, within the error margin. The error is large due to the value being the ratio of two measured parameters both having significant uncertainties. The next maximum in the histogram corresponds to an average count rate enhancement of 4.7 ± 2.2 . This is clearly beyond the theory prediction despite having a similarly large margin of error. Finally there is one diamond showing even higher count rate enhancement. The obtained statistics suggests the existence of an additional mechanism responsible for extra count rate enhancement. To get at least a qualitative understanding of this phenomenon we have employed an additional computational effort. For this, we assumed that excessive emission rates from certain nanodiamonds potentially could arise from the influence of either neighboring superlattice defects or adjacent “dark” nanodiamonds lacking NV centers. The proposed mechanism is as follows: HMMs can support surface plasmon-polaritons (SPPs) and bulk electromagnetic modes, both having high propagation constant (high-k modes) [68]. It is known that an excited emitter located in the vicinity of HMM surface has a high probability of transferring energy into such high-k modes [53]. Once excited, these modes propagate through the HMM never leaving its bulk where they are eventually absorbed and do not provide any contribution to the collected photon flux. However, the presence of the surface defects or scattering objects may result in outcoupling of these modes into the far field and therefore provide additional contribution to the emitted signal. We would like to note that thorough study on the role of the SPP and HMM high-k propagating modes in enhancing LDOS was reported in [42, 50].

To verify this assumption both substrate defects and “dark” nanodiamonds were modelled as 50-nm-diameter spheres with varied separation from emitting dipole. Calculations were performed using finite-element analysis (COMSOL Multiphysics) with detailed results given in the Supporting Information S6. In essence, the calculation indeed demonstrated that the presence of the dark nanodiamond and TiN particle results in further enhancements of emission rate by factors of 1.3 and 2.0, respectively compared to a perfect HMM surface. This result does support the experimental observations though it clearly requires further rigorous investigation. In particular, instead of relying on random irregularities of the HMM surface, one can try to place emitting nanodiamonds next to engineered nanostructures with optimized outcoupling efficiency. It is also worth noting that our calculation clearly shows that the portion of NV center emission coupled into the metamaterial could be quite efficiently recovered prior to dissipation in the HMM. This emission could be directed into the far-field by using even very basic structures, such as gratings, nanodisks, nanoholes, etc.

5. Conclusion and Outlook

We have experimentally demonstrated an improvement in the emission properties of single NV center nanodiamonds placed on top of an epitaxial, TiN/(Al,Sc)N HMM compared to a glass substrate. The observed lifetime decreased from 17 ns to 4.3 ns on average. This ratio corresponds to a Purcell factor of 4, which is in good agreement with theoretical prediction giving Purcell factor of 4.5. We have also found that the collected emission power for NV centers near the HMM was increased by a factor of 1.8 on average, although a quite remarkable enhancement of 4.7 was detected in one particular case. These results indicate that the brightness of the nanodiamond-based single-photon emitter could be substantially enhanced by placing such an emitter on the surface of a TiN/(Al,Sc)N hyperbolic metamaterial. Importantly, such placement is not location-specific and does not require nanodiamond manipulation. Bright single-photon emitters could be located within a reasonable time frame with a conventional microscope, and used for building highly efficient room temperature CMOS-compatible single-photon sources. The emission rate could be further enhanced by the presence of an adjacent HMM defect. This latter fact suggests the possibility of using a pre-fabricated nanostructure at the HMM surface optimized for outcoupling of high-k HMM modes that would otherwise propagate and eventually get absorbed inside the HMM.

Supporting Information

Additional supporting information may be found in the online version of this article at the publisher's website.

Acknowledgements. The authors would like to thank Nathaniel Kinsey for his help with manuscript preparation, Simeon Bogdanov, Jingjing Liu, Bivas Saha, and Viktoriia E. Babicheva for fruitful discussions. This work was partially supported by the AFOSR-MURI grant (FA9550-10-1-0264), ARO grant 57981-PH (W911NF-11-1-0359) and NSF-MRSEC grant (DMR-1120923).

Received: 7 August 2014, **Revised:** 20 October 2014,

Accepted: 11 November 2014

Published online: 12 December 2014

Key words: single-photon source, metamaterials, nitrogen-vacancy center, hyperbolic dispersion.

References

- [1] C. Monroe, *Nature* **416**(6877), 238–246 (2002).
- [2] D. P. DiVincenzo, *Science* **270**(5234), 255–261 (1995).
- [3] N. Gisin, G. Ribordy, and H. Zbinden, *arXiv Prepr. quant-ph/0101098* (2001).
- [4] L. M. Duan, M. D. Lukin, J. I. Cirac, and P. Zoller, *Nature* **414**, 413 (2001).
- [5] D. Bouwmeester, J. W. Pan, K. Mattle, M. Eibl, H. Weinfurter, and A. Zeilinger, *Nature* **390**(6660), 575–579 (1997).

- [6] M. D. Eisaman, J. Fan, A. Migdall, and S. V. Polyakov, *Rev. Sci. Instrum.* **82**(7), 071101 (2011).
- [7] M. Hennrich, T. Legero, A. Kuhn, and G. Rempe, *New J. Phys.* **6**(1), 86 (2004).
- [8] C. Maurer, C. Becher, C. Russo, J. Eschner, and R. Blatt, *New J. Phys.* **6**(1), 94 (2004).
- [9] M. Steiner, A. Hartschuh, R. Korlacki, and A. J. Meixner, *Appl. Phys. Lett.* **90**(18), 183122–183122 (2007).
- [10] E. Wu, J. R. Rabeau, G. Roger, F. Treussart, H. Zeng, P. Grangier, S. Praver, and J. F. Roch, *New J. Phys.* **9**(12), 434 (2007).
- [11] S. Chen, Y. A. Chen, T. Strassel, Z. S. Yuan, B. Zhao, J. Schmiedmayer, and J. W. Pan, *Phys. Rev. Lett.* **97**(17), 173004 (2006).
- [12] A. V. Akimov, A. Mukherjee, C. L. Yu, D. E. Chang, A. S. Zibrov, P. R. Hemmer, H. Park, and M. D. Lukin, *Nature* **450**, 402–406 (2007).
- [13] J. Kim, O. Benson, H. Kan, and Y. Yamamoto, *Nature* **397**(6719), 500–503 (1999).
- [14] A. Gruber, A. Dräbenstedt, C. Tietz, L. Fleury, J. Wrachtrup, and C. Von Borczyskowski, *Science* **276**(5321), 2012–2014 (1997).
- [15] C. Kurtsiefer, S. Mayer, P. Zarda, and H. Weinfurter, *Phys. Rev. Lett.* **85**(2), 290–293 (2000).
- [16] P. Tamarat, T. Gaebel, J. R. Rabeau, M. Khan, A. D. Green-tree, H. Wilson, L. C. L. Hollenberg, S. Praver, P. Hemmer, F. Jelezko, and J. Wrachtrup, *Phys. Rev. Lett.* **97**(8), 083002 (2006).
- [17] G. D. Fuchs, V. V. Dobrovitski, R. Hanson, A. Batra, C. D. Weis, T. Schenkel, and D. D. Awschalom, *Phys. Rev. Lett.* **101**(11), 117601 (2008).
- [18] T. A. Kennedy, J. S. Colton, J. E. Butler, R. C. Linares, and P. J. Doering, *Appl. Phys. Lett.* **83**(20), 4190–4192, (2003).
- [19] P. Neumann, J. Beck, M. Steiner, F. Rempp, H. Fedder, P. R. Hemmer, J. Wrachtrup, and F. Jelezko, *Science* **329**(5991), 542–544 (2010).
- [20] P. C. Maurer, G. Kucsko, C. Latta, L. Jiang, N. Y. Yao, S. D. Bennett, F. Pastawski, D. Hunger, N. Chisholm, M. Markham, D. J. Twitchen, J. I. Cirac, and M. D. Lukin, *Science* **336**(6086), 1283–1286 (2012).
- [21] L. Robledo, L. Childress, H. Bernien, B. Hensen, P. F. Alkemade, and R. Hanson, *Nature* **477**(7366), 574–578 (2011).
- [22] F. Dolde, I. Jakobi, B. Naydenov, N. Zhao, S. Pezzagna, C. Trautmann, J. J. Meijer, P. Neumann, F. Jelezko, and J. Wrachtrup, *Nat. Phys.* **9**(3), 139–143 (2013).
- [23] M. V. G. Dutt, L. Childress, L. Jiang, E. Togan, J. Maze, F. Jelezko, A. S. Zibrov, P. R. Hemmer, and M. D. Lukin, *Science* **316**(5829), 1312–1316 (2007).
- [24] F. Dolde, H. Fedder, M. W. Doherty, T. Nöbauer, F. Rempp, G. Balasubramanian, T. Wolf, F. Reinhard, L. C. L. Hollenberg, F. Jelezko, and J. Wrachtrup, *Nat. Phys.* **7**, 459–463 (2011).
- [25] J. R. Maze, P. Stanwix, J. S. Hodges, S. Hong, J. M. Taylor, P. Cappellaro, L. Jiang, M. V. Gurudev Dutt, E. Togan, A. S. Zibrov, A. Yacoby, R. L. Walsworth, and M. D. Lukin, *Nature* **455**, 644–648 (2008).
- [26] G. Kucsko, P. C. Maurer, N. Y. Yao, M. Kubo, H. J. Noh, P. K. Lo, H. Park, and M. D. Lukin, *Nature* **500**(7460), 54–58 (2013).
- [27] A. Ajoy and P. Cappellaro, *Phys. Rev. A* **86**(6), 062104 (2012).
- [28] T. Schröder, F. Gädeke, M. J. Banholzer, and O. Benson, *New J. Phys.* **13**(5), 055017 (2011).
- [29] J. P. Hadden, J. P. Harrison, A. C. Stanley-Clarke, L. Marseglia, Y. L. Ho, B. R. Patton, J. L. O’Brien, and J. G. Rarity, *Appl. Phys. Lett.* **97**(24), 241901 (2010).
- [30] T. M. Babinec, B. J. Hausmann, M. Khan, Y. Zhang, J. R. Maze, P. R. Hemmer, and M. Lončar, *Nat. Nanotechnol.* **5**(3), 195–199 (2010).
- [31] J. T. Choy, I. Bulu, B. J. Hausmann, E. Janitz, I. C. Huang, and M. Lončar, *Appl. Phys. Lett.* **103**(16), 161101 (2013).
- [32] E. M. Purcell, *Phys. Rev.* **69**, 681 (1946).
- [33] S. Schietinger and O. Benson, *J. Phys. B: At. Mol. Opt. Phys.* **42**(11), 114001 (2009).
- [34] J. Riedrich-Möller, L. Kipfstuhl, C. Hepp, E. Neu, C. Pauly, F. Mücklich, A. Baur, M. Wandt, S. Wolff, M. Fischer, S. Gsell, M. Schreck, and C. Becher, *Nat. Nanotechnol.* **7**(1), 69–74 (2012).
- [35] A. Faraon, C. Santori, Z. Huang, V. M. Acosta, and R. G. Beausoleil, *Phys. Rev. Lett.* **109**(3), 033604 (2012).
- [36] B. J. Hausmann, B. J. Shields, Q. Quan, Y. Chu, N. P. de Leon, R. Evans, M. J. Burek, A. S. Zibrov, M. Markham, D. J. Twitchen, H. Park, M. D. Lukin, and M. Lončar, *Nano Lett.* **13**(12), 5791–5796 (2013).
- [37] D. R. Smith and D. Schurig, *Phys. Rev. Lett.* **90**(7), 077405 (2003).
- [38] Z. Jacob, L. V. Alekseyev, and E. Narimanov, *Opt. Express* **14**(18), 8247–8256 (2006).
- [39] A. Poddubny, I. Iorsh, P. Belov, and Y. Kivshar, *Nat. Photonics* **7**(12), 948–957 (2013).
- [40] Z. Liu, H. Lee, Y. Xiong, C. Sun, and X. Zhang, *Science* **315**(5819), 1686–1686 (2007).
- [41] M. A. Noginov, H. Li, Y. A. Barnakov, D. Dryden, G. Nataraj, G. Zhu, C. E. Bonner, M. Mayy, Z. Jacob, and E. E. Narimanov, *Opt. Lett.* **35**(11), 1863–1865 (2010).
- [42] J. Kim, V. P. Drachev, Z. Jacob, G. V. Naik, A. Boltasseva, E. E. Narimanov, and V. M. Shalaev, *Opt. Express* **20**(7), 8100–8116 (2012).
- [43] D. Lu, J. J. Kan, E. E. Fullerton, and Z. Liu, *Nat. Nanotechnol.* **9**(1), 48–53 (2014).
- [44] Z. Jacob, J. Y. Kim, G. V. Naik, A. Boltasseva, E. E. Narimanov, and V. M. Shalaev, *Appl. Phys. B* **100**(1), 215–218 (2010).
- [45] H. N. Krishnamoorthy, Z. Jacob, E. Narimanov, I. Kretzschmar, and V. M. Menon, *Science* **336**(6078), 205–209 (2012).
- [46] L. Ferrari, D. Lu, D. Lepage, and Z. Liu, *Opt. Express* **22**(4), 4301–4306 (2014).
- [47] T. Galfsky, H. N. Krishnamoorthy, W. D. Newman, E. Narimanov, Z. Jacob, and V. M. Menon, “Directional out-coupling from active hyperbolic metamaterials,” *arXiv Prepr. arXiv1404.1535*, 2014.
- [48] M. Y. Shalaginov, S. Ishii, J. Liu, J. Irudayaraj, A. Lagutchev, A. V. Kildishev, and V. M. Shalaev, *Appl. Phys. Lett.* **102**(17), 173114 (2013).
- [49] G. V. Naik, V. M. Shalaev, and A. Boltasseva, *Adv. Mater.* **25**(24), 3264–3294 (2013).

- [50] G. V. Naik, B. Saha, J. Liu, S. M. Saber, E. A. Stach, J. M. Irudayaraj, T. D. Sands, V. M. Shalaev, and A. Boltasseva, *Proc. Natl. Acad. Sci. U. S. A.* **111**(21), 7546–7551 (2014).
- [51] G. V. Naik, J. L. Schroeder, X. Ni, A. V. Kildishev, T. D. Sands, and A. Boltasseva, *Opt. Mater. Express* **2**(4), 478–489 (2012).
- [52] U. Guler, A. Boltasseva, and V. M. Shalaev, *Science* **344**(6181), 263–264 (2014).
- [53] Z. Jacob, I. I. Smolyaninov, and E. E. Narimanov, *Appl. Phys. Lett.* **100**(18), 181105 (2012).
- [54] O. Kidwai, S. V. Zhukovsky, and J. E. Sipe, *Opt. Lett.* **36**(13), 2530–2532 (2011).
- [55] C. Bradac, T. Gaebel, N. Naidoo, J. R. Rabeau, and A. S. Barnard, *Nano Lett.* **9**(10), 3555–3564 (2009).
- [56] S. Mahendia, A. K. Tomar, R. P. Chahal, P. Goyal, and S. Kumar, *J. Phys. D Appl. Phys.* **44**(20), 205105 (2011).
- [57] J. Elser, V. A. Podolskiy, I. Salakhutdinov, and I. Avrutsky, *Appl. Phys. Lett.* **90**(19), 191109 (2007).
- [58] R. M. A. Azzam and N. M. Bashara, *Ellipsometry and polarized light* (Elsevier Science Publishing Co., Inc., North-Holland, 1987).
- [59] D. O'Connor and D. Phillips, *Time-correlated Single Photon Counting*, (Academic Press, London, 1984).
- [60] R. H. Brown and R. Q. Twiss, *Nature* **177**(4497), 27–29 (1956).
- [61] A. Beveratos, R. Brouri, T. Gacoin, J. P. Poizat, and P. Grangier, *Phys. Rev. A* **64**(6), 061802 (2001).
- [62] M. S. Yeung and T. K. Gustafson, *Phys. Rev. A* **54**(6), 5227–5242 (1996).
- [63] J. E. Sipe, *Surf. Sci.* **5**, 489–504 (1981).
- [64] G. W. Ford and W. H. Weber, *Phys. Rep.* **113**(4), 195–287 (1984).
- [65] L. Novotny and B. Hecht, *Principles of Nano-Optics* (Cambridge University Press, Cambridge, England, 2006).
- [66] C. L. Cortes, W. Newman, S. Molesky, and Z. Jacob, *J. Opt.* **14**(6), 063001 (2012).
- [67] K. Visscher, G. J. Brakenhoff, and T. D. Visser, *J. Microsc.* **175**(2), 162–165 (1994).
- [68] S. V. Zhukovsky, O. Kidwai, and J. E. Sipe, *Opt. Express* **21**(12), 14982–14987 (2013).

Supporting Information

Enhancement of single photon emission from nitrogen-vacancy centers with TiN/(Al,Sc)N hyperbolic metamaterial

M. Y. Shalaginov^{1,2,*}, V. V. Vorobyov^{3,4,*}, J. Liu⁵, M. Ferrera^{1,2,7}, A. V. Akimov^{4,6,8},
A. Lagutchev², A. N. Smolyaninov³, V. V. Klimov^{3,8}, J. Irudayaraj⁵, A. V. Kildishev^{1,2},
A. Boltasseva^{1,2} and V. M. ShalaeV^{1,2,†}

¹*School of Electrical and Computer Engineering, Purdue University, West Lafayette, IN 47907, USA*

²*Birck Nanotechnology Center, Purdue University, West Lafayette, IN 47907, USA*

³*Photonic Nano-Meta Technologies, ul. Lugovaya 4, Skolkovo Innovation Center, Moscow, 143026, Russia*

⁴*Moscow Institute of Physics and Technology, Institutskiy per. 9, Dolgoprudny, Moscow Region, 141700, Russia*

⁵*Agricultural and Biological Engineering, Purdue University, West Lafayette, IN 47907, USA*

⁶*Russian Quantum Center, ul. Novaya 100, BC "Ural", Skolkovo Innovation Center, Moscow Region, 143025, Russia*

⁷*School of Engineering and Physical Sciences, Heriot-Watt University, Edinburgh, Scotland EH14 4AS, United Kingdom*

⁸*Lebedev Physical Institute RAS, Leninskij pr. 53, Moscow, 119991, Russia*

* These authors contributed equally to this work.

† Electronic mail: shalaeV@purdue.edu

S1. Retrieval of dielectric functions

The multilayer metamaterial was characterized by a variable angle spectroscopic ellipsometer (J. A. Woollam Co.; W-VASE). The dielectric functions of the constituent materials (TiN and Al_{0.7}Sc_{0.3}N) as well as substrate (MgO) were retrieved from values Ψ and Δ measured in the wavelength range 300 – 2000 nm at angles of incidence 50° and 70°. The Drude-Lorentz model used for fitting is the following:

$$\varepsilon(\hbar\omega) = \varepsilon_1 + i\varepsilon_2 = \varepsilon_\infty + \sum_k \frac{A_k}{E_k^2 - (\hbar\omega)^2 - iB_k\hbar\omega} \quad \text{S(1)}$$

where \hbar is the reduced Plank's constant, A_k is the amplitude, E_k is the center energy and B_k is the broadening of each oscillator [1].

Table S1. Experiment-fitted parameters of the Drude-Lorentz model for (Al,Sc)N and TiN films.

	TiN	(Al,Sc)N
ε_∞	4	4
A_1 (eV) ²	52.536	0
B_1 (eV)	0.29197	0
A_2 (eV) ²	130.93	11.162
B_2 (eV)	4.9807	0.63261
E_2 (eV)	5.9784	3.6857

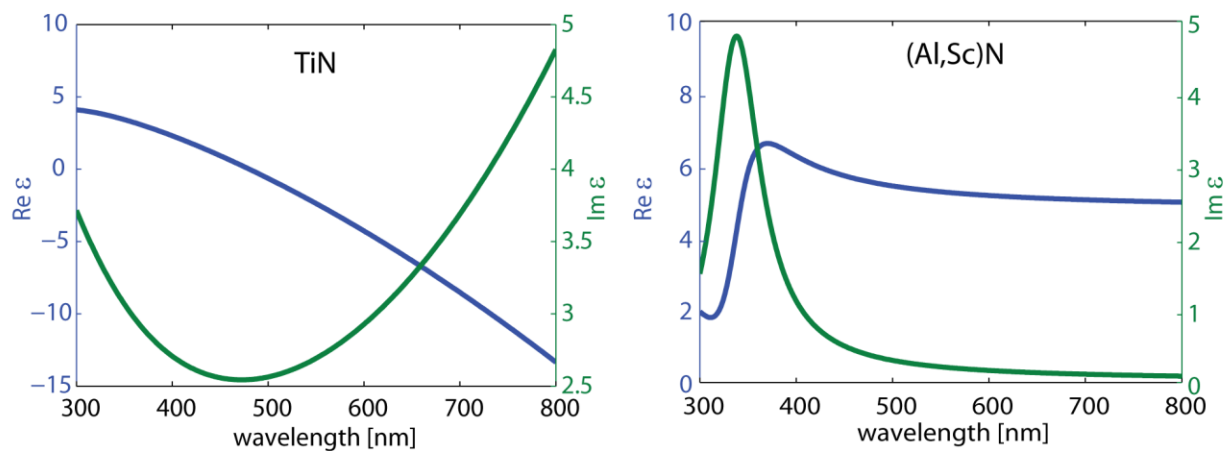


Fig. S1. The dielectric functions of TiN and (Al,Sc)N: real and imaginary parts are shown with blue and green lines, respectively.

S2. Transmittance, reflectance, and absorbance of the HMM sample

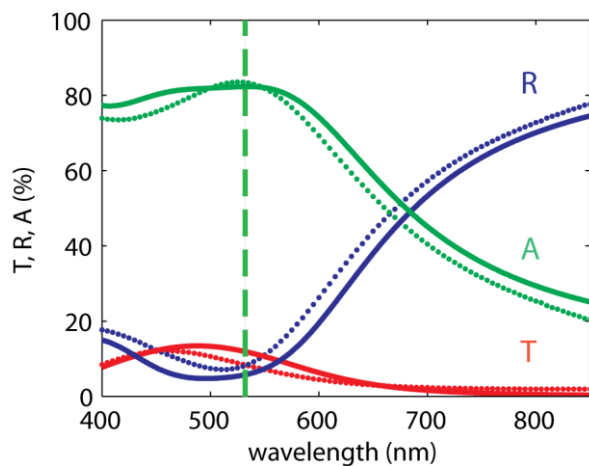


Fig. S2. Transmittance (T), reflectance (R), and absorbance (A) of the TiN HMMs calculated using direct T-matrix method (solid line) [2] and measured by spectrophotometry (dotted line); angle of incidence for T – 0°, for R – 8°; $A = 1 - T - R$.

S3. Semi-analytical calculations of Purcell effect and normalized collected emission power

A single emitter is modeled as an oscillating electric dipole with dipole moment \mathbf{p} and angular frequency ω . The dipole rate of energy dissipation in an inhomogeneous environment is given by [3]

$$P = \frac{\omega}{2} \text{Im}[\mathbf{p}^* \cdot \mathbf{E}_0(\mathbf{r}_0) + \mathbf{E}_s(\mathbf{r}_0)] \quad \text{S(2)}$$

where $\mathbf{E}_0(\mathbf{r}_0)$ and $\mathbf{E}_s(\mathbf{r}_0)$ are the primary dipole field and the scattered field at the dipole position \mathbf{r}_0 , respectively. The electric fields were calculated using the dyadic Green's function formalism [3]. Utilizing angular spectrum representation of the Green's functions allowed us to analyze the contribution of each spatial frequency mode (k-mode).

For a single dipole emitter with in-plane (\parallel) or perpendicular (\perp) orientation placed at a distance h above a multilayer planar structure, the corresponding Purcell factors F_P can be calculated using the following formulas [3]

$$F_P^\perp = 1 + \frac{3}{2} \frac{1}{\epsilon_{\text{sup}}^{3/2}} \int_0^\infty \text{Re} \left\{ \frac{s^3}{s_{\perp, \text{sup}}(s)} \tilde{r}^p(s) e^{2ik_0 s_{\perp, \text{sup}}(s)h} \right\} ds, \quad \text{S(3)}$$

$$F_P^\parallel = 1 + \frac{3}{4} \frac{1}{\epsilon_{\text{sup}}^{1/2}} \int_0^\infty \text{Re} \left\{ \frac{s}{s_{\perp, \text{sup}}(s)} \left[\tilde{r}^s(s) - \frac{s_{\perp, \text{sup}}^2(s)}{\epsilon_{\text{sup}}} \tilde{r}^p(s) \right] e^{2ik_0 s_{\perp, \text{sup}}(s)h} \right\} ds, \quad \text{S(4)}$$

The value of F_P for the statistically averaged (ave) dipole orientation is given by

$$F_P^{\text{ave}} = \frac{2}{3} F_P^\parallel + \frac{1}{3} F_P^\perp. \quad \text{S(5)}$$

Normalized collected emission powers f_{rad} for the same dipole orientations are shown below

$$f_{rad}^{\perp} = \frac{3}{4} \int_0^{\theta_{\max}} \sin^3 \theta \left| e^{-i\varepsilon_{\text{sup}}^{1/2} k_0 h \cos \theta} + \tilde{r}^p(\theta) e^{i\varepsilon_{\text{sup}}^{1/2} k_0 h \cos \theta} \right|^2 d\theta, \quad \text{S(6)}$$

$$f_{rad}^{\parallel} = \frac{3}{8} \int_0^{\theta_{\max}} \cos^2 \theta \left| e^{-i\varepsilon_{\text{sup}}^{1/2} k_0 h \cos \theta} - \tilde{r}^p(\theta) e^{i\varepsilon_{\text{sup}}^{1/2} k_0 h \cos \theta} \right|^2 + \left| e^{-i\varepsilon_{\text{sup}}^{1/2} k_0 h \cos \theta} + \tilde{r}^s(\theta) e^{i\varepsilon_{\text{sup}}^{1/2} k_0 h \cos \theta} \right|^2 \sin \theta d\theta, \quad \text{S(7)}$$

$$f_{rad}^{ave} = \frac{2}{3} f_{rad}^{\parallel} + \frac{1}{3} f_{rad}^{\perp}. \quad \text{S(8)}$$

In equations S(3) - S(8), $s = k_{\parallel}/k_0$, $s_{\perp, \text{sup}}(s) = k_{\perp, \text{sup}}(s)/k_0 = \varepsilon_{\text{sup}} - s^2$ ^{1/2}, $k_0 = \omega/c$, θ is a polar angle measured from the \perp direction, the collection angle $\theta_{\max} = 79.6^\circ$. The integrals are numerically evaluated by using an adaptive Gauss–Kronrod quadrature method [4]. In the formulas, we assume that the intrinsic quantum yield of NV centers is close to unity.

S4. Calculation of generalized reflection and transmission coefficients of a planar multilayer slab

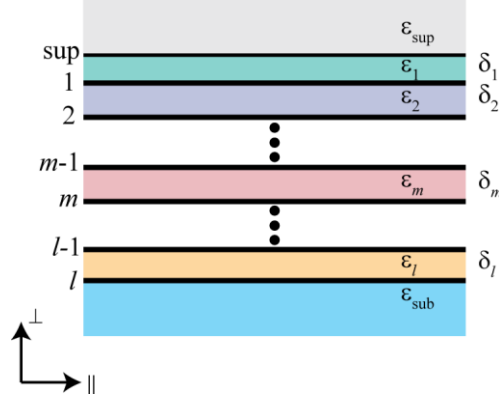


Fig. S3. Schematic of an arbitrary planar lamellar slab consisting of l layers.

We use a recursive invariant imbedding [5] to compute generalized reflection coefficients $\tilde{r}^{(p,s)}$ that incorporate the reflection from the m -th interface (interface between m -th and $m+1$ -th layer) and all the subsequent reflections from the interfaces positioned below. The schematic of the structure is shown in Fig. S3. Each layer is characterized by relative permittivity ϵ_m and thickness δ_m . Above and below the multilayer slab, there are half-spaces of superstrate (ϵ_{sup}) and substrate (ϵ_{sub}), respectively. The iterative formula to calculate $\tilde{r}^{(p,s)}(s)$ is the following

$$\tilde{r}_m^{(p,s)}(s) = \frac{r_m^{(p,s)}(s) + \tilde{r}_{m+1}^{(p,s)}(s)e^{i2k_0s_{\perp,m}(s)\delta_m}}{1 + r_m^{(p,s)}(s)\tilde{r}_{m+1}^{(p,s)}(s)e^{i2k_0s_{\perp,m}(s)\delta_m}}, \quad m \in \overline{\text{sup}, 1, l}, \quad \text{S(9)}$$

where $s_{\perp,m} = k_{\perp,m}/k_0 = \epsilon_m - s^2$ ^{1/2}, where $r_m^{(p,s)}$ are the conventional single-interface Fresnel coefficients

$$r_m^p(s) = \frac{\varepsilon_m s_{\perp, m-1}(s) - \varepsilon_{m-1} s_{\perp, m}(s)}{\varepsilon_m s_{\perp, m-1}(s) + \varepsilon_{m-1} s_{\perp, m}(s)}, \quad r_m^s(s) = \frac{s_{\perp, m-1}(s) - s_{\perp, m}(s)}{s_{\perp, m-1}(s) + s_{\perp, m}(s)}. \quad \text{S(10)}$$

The iteration starts from the substrate ($\tilde{r}_{l+1}^{(p,s)}(s) = 0$), then we come up with the seeding iteration ($\tilde{r}_l^{(p,s)}(s) = r_l^{(p,s)}(s)$) and continue with the next step:

$$\tilde{r}_{l-1}^{(p,s)}(s) = \frac{r_{l-1}^{(p,s)}(s) + r_l^{(p,s)}(s)e^{i2k_0 s_{\perp, l-1}(s)\delta_{l-1}}}{1 + r_{l-1}^{(p,s)}(s)r_l^{(p,s)}(s)e^{i2k_0 s_{\perp, l-1}(s)\delta_{l-1}}}. \quad \text{S(11)}$$

It should be noted that S(11) can be turned into the familiar Drude formula for the reflection coefficient for a single layer of thickness δ [6]:

$$r^{(p,s)}(s) = \frac{r_{1,2}^{(p,s)}(s) + r_{2,3}^{(p,s)}(s)e^{i2k_0 s_{\perp}(s)\delta}}{1 + r_{1,2}^{(p,s)}(s)r_{2,3}^{(p,s)}(s)e^{i2k_0 s_{\perp}(s)\delta}}. \quad \text{S(12)}$$

In the formulas S(6) and S(7), \tilde{r}^p and \tilde{r}^s are expressed as functions of a polar angle θ instead of normalized in-plane wavevector s . The relation between s and θ for the modes propagating in the superstrate medium is $s(\theta) = \varepsilon_{\text{sup}}^{1/2} \sin(\theta)$.

S5. Dependence of emission characteristics on dipole moment orientation and the distance between an emitter and HMM surface

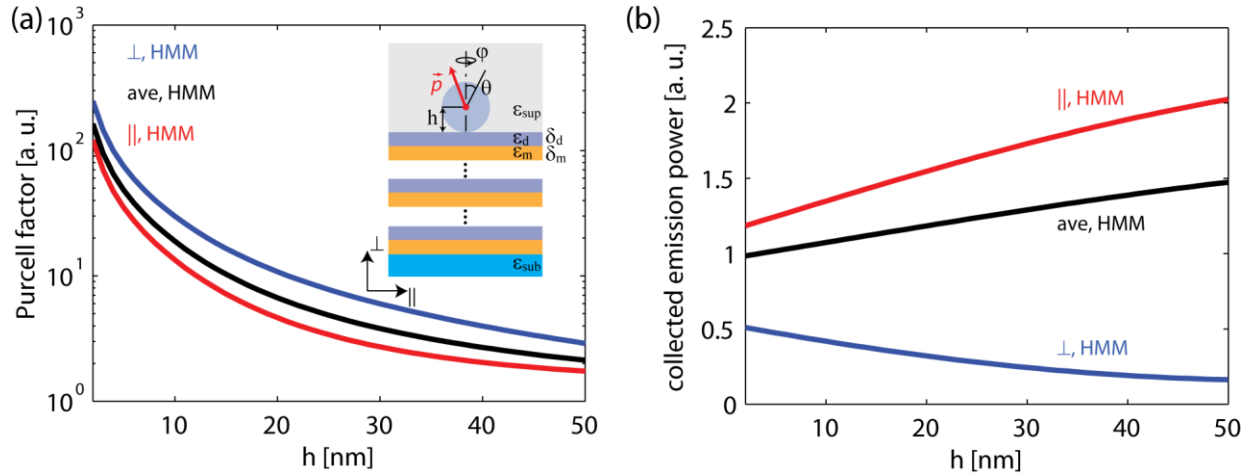


Fig. S4. Dependence of the Purcell factor F_P and the collected emission power f_{rad} on a dipole position h above the HMM surface. Values of F_P and f_{rad} are obtained by averaging the characteristics (shown in Fig. 3 in the main text) over the wavelength range 600-800 nm.

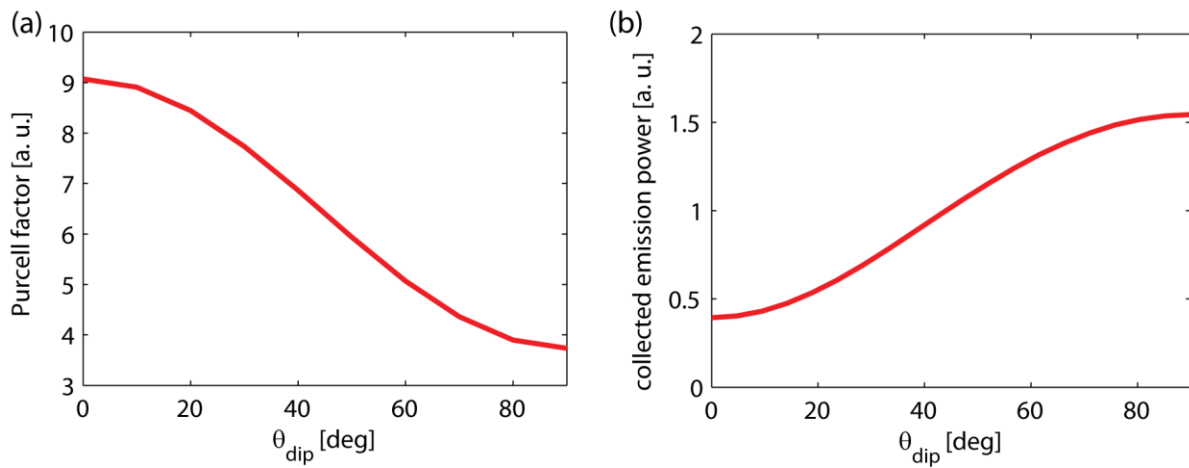


Fig. S5. Dependence of the Purcell factor and the collected emission power on orientation of the emitter's dipole moment. θ_{dip} is a polar angle of the dipole orientation measured from the \perp direction.

S6. Influence of neighboring nanodiamonds and structural surface defects of HMM on collected emission power

We have studied the influence of surface superlattice defects and nanodiamonds (NDs) lacking NV centers on collected emission power. Examples of the defects and agglomerated NDs are shown in Fig. 6(a). To qualitatively estimate the influence of these scattering objects, we have performed finite-element method (FEM) analysis using a commercial numerical simulation tool (COMSOL Multiphysics). The schematic of the simulated structure is shown in Fig. 6(b). The HMM is considered as effective anisotropic medium, where scatterers are modelled as either diamond or TiN spheres of 50 nm in diameter. The emitter is emulated by an electric point dipole embedded into 50-nm-diameter diamond sphere. The superstrate and substrate are respectively the immersion oil and MgO. The distance between the emitter and the scatter was taken to be 10 nm, 69 nm, and 343 nm. The emission wavelength was fixed to 685 nm.

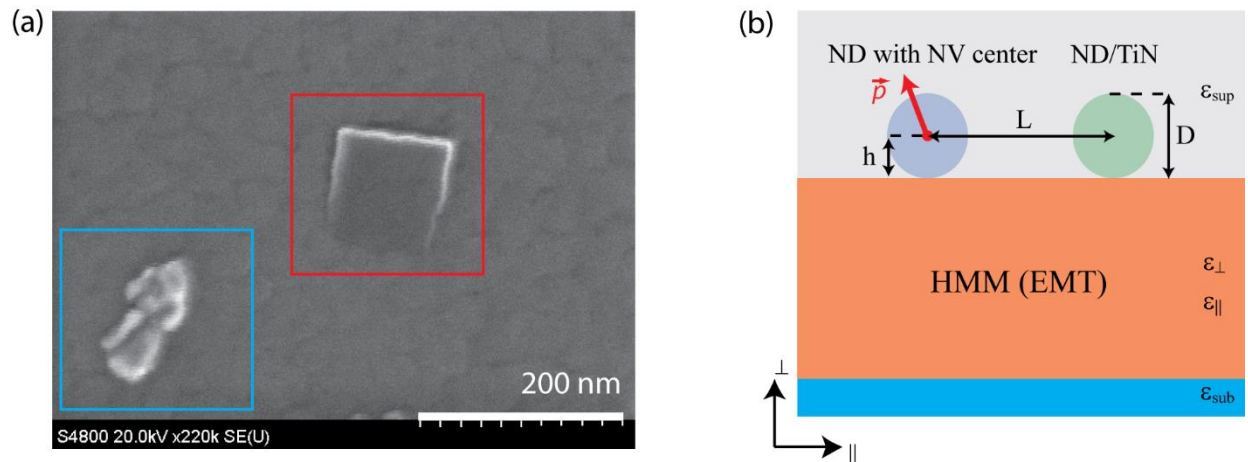


Fig. S6. (a) SEM scan showing a superlattice defect (inside red frame) and agglomerated NDs (inside blue frame). (b) Schematic of the simulated structure.

Results of the FEM simulations are summarized in Table S2. All values of the collected emission powers are normalized by the corresponding powers emitted by the dipole source located on top of the glass coverslip. The noticeable influence is observed at small separation distances (less than 50 nm). For a statistically averaged dipole orientation, an adjacent (at a distance ~ 10 nm) ND or structural surface defect can increase the collected emission power by 30% or 200%, respectively. For an in-plane oriented emitter, the increase in emitted power from a nearby surface defect could be up to 220%, giving an overall emission enhancement factor of 4. The comparison of the results obtained by using a semi-analytical approach and FEM analysis is shown in Fig. .

Table S2. Influence of NDs lacking NV centers and structural surface defects (TiN particles) on normalized collected emission power.

	on HMM	on HMM with ND			on HMM with TiN particle		
		10 nm	69 nm	343 nm	10 nm	69 nm	343 nm
in-plane (\parallel)	1.8	2.3	1.8	1.8	3.9	1.9	1.8
perpendicular (\perp)	0.6	0.6	0.6	0.6	0.2	0.4	0.6
averaged (ave)	1.5	1.9	1.5	1.5	3.0	1.5	1.5

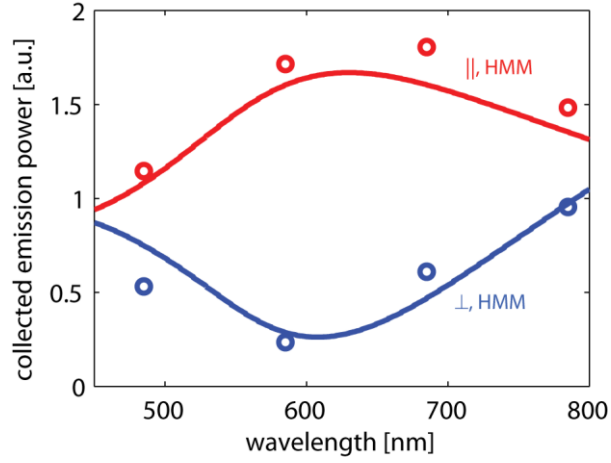


Fig. S7. Agreement between semi-analytical (solid line) and FEM calculations (circles). The calculations are performed for the HMM without any scatterers. Blue and red curves correspond to the dipole orientations perpendicular (\perp) and parallel (\parallel) to the HMM interface, respectively.

References

- [1] Guide to Using WVASE 32: Spectroscopic Ellipsometry Data Acquisition and Analysis Software, J. A. Woollam Company, Incorporated, 2008.
- [2] P. Yeh, Optical waves in layered media (Wiley, New York, 1988).
- [3] L. Novotny and B. Hecht, Principles of Nano-Optics (Cambridge University Press, Cambridge, England, 2006).
- [4] L. F. Shampine, J. Comput. Appl. Math., **211**, **2**, 131-140, (2008).
- [5] W. C. Chew and S. Y. Chen, Antennas Wirel. Propag. Lett., **2**, **1**, 254-258 (2003).
- [6] P. Drude, Ann. Phys., **272**, 865-897 (1889).